PHYSICAL REVIEW B **82**, 184417 (2010)

Structure and magnetic properties of MnSi epitaxial thin films

E. Karhu, S. Kahwaji, and T. L. Monchesky
Department of Physics and Atmospheric Science, Dalhousie University, Halifax, Nova Scotia, Canada B3H 3J5

C. Parsons and M. D. Robertson
Department of Physics, Acadia University, Wolfville, Nova Scotia, Canada B4P 2R6

C. Maunders
Materials Science and Engineering, McMaster University, Hamilton, Ontario, Canada L8S 4L7

(Received 30 August 2010; revised manuscript received 21 October 2010; published 12 November 2010)

We report on the correlation between the magnetic and structural properties of epitaxial MnSi (111) thin films grown by solid-phase epitaxy on Si (111) substrates. The Si (111) substrate, with a surface unit cell that is 3.0% larger than that of MnSi, causes an in-plane tensile strain in the film that is partially relaxed due to the presence of misfit dislocations located at the interface. However, the out-of-plane strain has a nonmonotonic dependence on thickness that is attributed to changes in the elastic constants of the film. The thickness dependence of the Curie temperature correlates strongly with strain and reaches a maximum of $T_C=43$ K, a value that is 46% greater than the bulk value of $T_C=29.5$ K. Although the films have a strong epitaxial relationship, $[1\bar{1}0]$MnSi$\parallel$$[11\bar{2}]$Si, there are inversion domains in the film due to the noncentrosymmetric crystal structure of MnSi. The presence of these domains implies that there are two magnetic chiralities, which likely contribute to the observed glassy magnetic response of the films.

DOI: 10.1103/PhysRevB.82.184417 PACS number(s): 75.70.Ak, 75.30.Cr, 68.37.Lp, 68.60.Bs

I. INTRODUCTION

Thin-film heterostructures that combine ferromagnetic, antiferromagnetic, and nonmagnetic materials play a central role in spintronics research and constitute the building blocks for spin valves and magnetic tunnel junctions. However, only recently have noncollinear magnetic structures been considered in the context of spintronics. Helical magnets are one class of noncollinear structures that have been identified as interesting materials for spin-dependent electron transport studies. Several effects, such as dissipationless spin currents[1] and spin-transfer-torque-induced rotation of the helical order parameter,[2] are predicted in these materials. Heterostructures based on thin films of MnSi are an interesting system to explore some of these predictions, and furthermore, they offer an opportunity to explore a skyrmion phase with unique transport properties that has been recently identified in MnSi bulk samples.[3–5]

Bulk MnSi is a weak itinerant-electron helical magnet with a B20 crystal structure and a lattice parameter of $a_{\mathrm{MnSi}}=0.4561$ nm at room temperature.[6] At ambient pressure, the material orders magnetically below a Curie temperature of $T_C=29.5$ K. MnSi is nearly ferromagnetic: the Dzyaloshinskii-Moriya interaction, caused by the lack of inversion symmetry of the B20 crystal structure, destabilizes the ferromagnetism and produces a helical magnetic structure with the spins oriented perpendicular to the propagation vector, $\mathbf{Q}$. The wavelength of the helix is $2\pi/Q=18$ nm with $\mathbf{Q}$ parallel to $[111]$. In an external magnetic field, $\mathbf{Q}$ rotates in the direction of the field and becomes parallel to it at $H_{C1}\approx 0.1$ T. Above H_{C1}, a conical phase forms, which collapses into a ferromagnetic phase above $H_{C2}=0.6$ T.[7,8]

The ordering temperature decreases with increasing pressure up to a critical pressure of $p_c=1.48$ GPa, above which long-range magnetic order disappears.[9] Partial magnetic order exists in the neighborhood of p_c (Refs. 10 and 11) but the nature of this order remains an open question for which a number of models have been put forward,[12–14] including the existence of a glassy phase.[15]

Epitaxially induced strain in MnSi thin films provides a means of exploring pressure induced changes in magnetic structure. Silicon substrates (lattice parameter $a_{\mathrm{Si}}=0.5431$ nm) serve as suitable templates for MnSi growth. For growth of MnSi on Si (111), the lattice mismatch between MnSi (111) and Si (111) is $[a_{\mathrm{MnSi}}\cos(30°)-a_{\mathrm{Si}}]/a_{\mathrm{Si}}=-3.0\%$, when MnSi $[1\bar{1}0]$ is parallel to Si$[11\bar{2}]$. The large tensile strain induced by the substrate is expected to have an appreciable effect on the magnetic properties of the film since a compressive strain of only a few tens of a percent produces novel magnetic phases in bulk MnSi.[10]

A number of research groups have investigated manganese silicide thin films on Si (111) from a submonolayer layer to films as thick as 200 nm. In particular, during solid-state epitaxy, manganese is typically deposited onto Si (111) at room temperature and then annealed under ultrahigh-vacuum conditions. When annealed at temperatures as low as 250 °C, Mn films that are 3 ML thick, where 1 ML$=7.82\times 10^{14}$ atoms/cm^2 is defined by the Si (111) substrate, produce islands with a $\sqrt{3}\times\sqrt{3}$ superstructure[16,17] corresponding to MnSi.[18] The crystallographic orientation of these islands was determined to be (111)Si$\parallel$(111)MnSi, $(1\bar{1}0)$Si$\parallel$$(11\bar{2})$MnSi.[19] For Mn layers thicker than 4 ML, MnSi thin films have holes,[16,20] which were believed to act as either local strain relief or serve as a silicon source for MnSi formation. Care must be taken during the annealing stage of solid-phase epitaxy since it has been reported that temperatures greater than 600 °C can transform the MnSi films into MnSi$_{1.7}$.[21] However, we have observed that it was possible to transform some of the MnSi into MnSi$_{1.7}$ at temperatures as low as 400 °C when annealed for 16 h.

In contrast to bulk MnSi, the magnetic properties of MnSi thin films have remained largely unexplored. Magneto-optic Kerr effect measurements on MnSi films show the existence of magnetic order but the low signal to noise in the measurements prevented accurate determination of T_C.[22] Magnano *et al.*[23] recently reported superconducting quantum interference device (SQUID) measurements on Ag/24 nm MnSi/Si (111) with one $T_C \sim 30$ K attributed to helical magnetic order and a second $T_C > 300$ attributed to a ferromagnetic phase at the MnSi/Si interface. However, our measurements performed on Si/MnSi/Si (111) films display a more homogeneous behavior with only one T_C that is comparable to bulk MnSi, which suggests that the ferromagnetic phase reported by Magnano may be related to the Ag/MnSi interface.

In this paper we present the structural and magnetic properties of crystalline epitaxial MnSi films grown by solid-phase epitaxy on Si (111) in order to address the question of the effects of strain on the magnetic properties. We show that the epitaxially induced tensile strain results in an increase in the unit-cell volume as determined by x-ray diffraction (XRD) and transmission electron microscopy (TEM) measurements. The observed atypical strain relaxation behavior is correlated with the magnetic response measured by SQUID magnetometry. Unlike bulk crystals, there is an appreciable remanent magnetization due to the finite thickness of the film, which displays glassy behavior that can be explained by relaxation over a broad distribution of activation barriers.

II. FILM GROWTH AND STRUCTURAL CHARACTERIZATION

Boron doped Si(111) ± 0.5° wafers with a resistivity of 1–20 Ω cm were used as substrates. The substrates were degreased in acetone and methanol ultrasonic baths, rinsed in deionized water, and the native oxide was removed with a modified RCA cleaning procedure consisting of a 70 °C solution of NH_4OH, H_2O_2 and deionized water in a ratio of 1:2:10. The wafer was etched in the solution for 15 min, rinsed again in deionized water, blown dry with nitrogen, and then immediately loaded into a VG-V80 SiGe molecular beam epitaxy chamber. The base pressure of the system was less than 4×10^{-11} Torr. The silicon-oxide layer was removed by heating to 800 °C for 1 h and then the wafer was cooled to room temperature at a rate of less than 1 °C/s. Reflection high-energy electron diffraction (RHEED) patterns showed a sharp 7 × 7 reconstruction, consistent with a high-quality surface.

A series of Mn films were evaporated from an effusion cell onto clean Si surfaces at room temperature. The Mn flux rate was measured with Bayard-Alpert-type ionization gauge. Subsequent solid-phase reaction of the Mn with the Si was performed by heating the substrate in UHV at 400 °C under RHEED observation until a well-ordered RHEED pattern was achieved. For an 11.5-nm-thick MnSi film, the layer was annealed at 400 °C for 1 h, which crystallized the overlayer and yielded a $\sqrt{3} \times \sqrt{3}$ pattern characteristic of MnSi on Si (111).[20] The samples were then allowed to cool to 40 °C before a protective layer of amorphous silicon was deposited onto the surface. *Ex situ* x-ray reflectivity (XRR) confirms that the MnSi film is twice the thickness of the amorphous Mn films as expected.

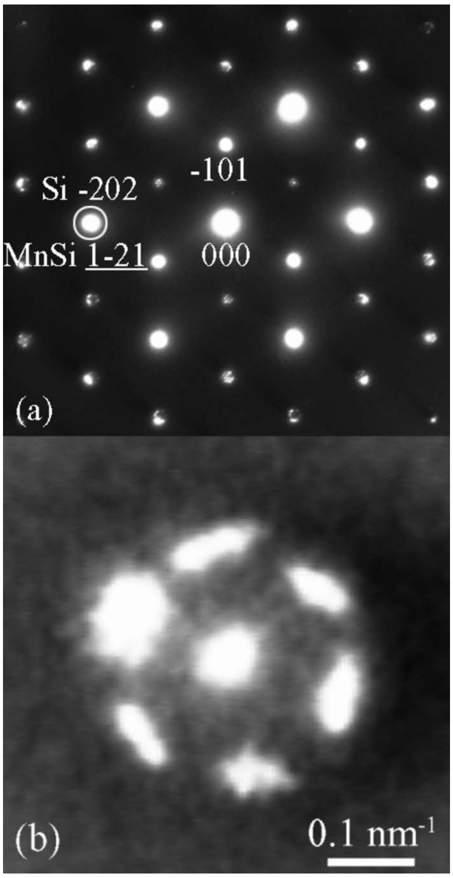

FIG. 1. (a) Planview SADP of an 11.5-nm-thick MnSi layer on a Si substrate at the [111] zone-axis orientation. (b) An expanded view of the diffraction spot circled in (a).

The structure of the MnSi layer was characterized by XRR, x-ray diffraction, and TEM. The high-resolution TEM (HRTEM) images were recorded using a 300 kV FEI Titan Cubed TEM (aberration corrected), and diffraction contrast imaging and selected-area electron-diffraction patterns (SADPs) were obtained using a 300 kV Philips TEM. Planview and cross-sectional specimens were prepared by low-angle mechanical polishing[24] without ion milling in order to minimize image artifacts as a result of preparation damage.

Presented in Fig. 1(a) is a SADP of a plan-view sample oriented at the [111] zone axis for a MnSi layer thickness of 11.5 nm on the Si substrate. Unless otherwise indicated, all indices refer to the MnSi layer. The inner ring of spots is due to diffraction from the {110} planes of MnSi and the bright second ring of spots results from diffraction from both Si {202} and MnSi {121} planes. The expected epitaxial orientation of $(111)\mathrm{Si}\|(111)\mathrm{MnSi}$ with $[1\bar{1}0]\mathrm{Si}\|[11\bar{2}]\mathrm{MnSi}$ is observed. There is fine structure present in each of the main diffraction spots and by enlarging the region circled in Fig. 1(a) the diffraction pattern as given in Fig. 1(b) is obtained. Each main diffraction spot is composed of a central spot surrounded by six symmetrically oriented spots generated as a result of double diffraction. The sample was oriented in the TEM such that the electron beam was incident on the MnSi layer first. Next, each MnSi diffracted spot acted as a source electron beam for the Si crystalline substrate and a complete [111] Si zone-axis diffraction pattern was generated for each MnSi spot (double-diffraction effect). If the MnSi layer was coherently strained to the Si substrate, the two materials would have the same in-plane lattice parameters, and all seven spots would overlap in a single spot. The reciprocal distance between the central spot and the outer ring of spots, Δg, can be related to the residual in-plane strain, $\varepsilon_{\|}$, in the layer by,

$$\varepsilon_{\|}(\%) = 3.0\% - 100\% \frac{\Delta g}{g_{ref}}, \qquad (1)$$

where the reciprocal distance from the (000) spot to one of the Si {220} reflections, g_{ref}, serves as an internal calibration standard. This method was used to quantify the relaxation of the in-plane strain as a function of MnSi layer thickness and corresponds to the data points shown in Fig. 5(a). A discussion of the strain results will be given later in this section.

The MnSi films appear to be uniform with very few precipitates or stacking-type defects present as shown in the low-magnification bright-field TEM image recorded at the [111] zone-axis orientation displayed in Fig. 2(a) for a 6-nm-thick MnSi layer. The dark bands and lines correspond to thickness fringe and bend contours, respectively, and the circular objects and blotches were due to polishing residue since the specimens were not ion milled. In order to visualize the chiral domains, the sample was tilted by about 16° so that the MnSi layer and the Si substrate were oriented close to the [221] and [112] zone axes, respectively, which produced the SADP is shown in Fig. 2(b). The dark-field image resulting from using the $(\bar{1}02)$ reflection is displayed in Fig. 2(c), where micron-sized domains appear bright. In fact, the SADP of Fig. 2(b) was obtained from one of the bright domains. Similarly, when a SADP was recorded from one of the dark regions in Fig. 2(c), then the SADP shown in Fig. 2(d) was obtained and the dark-field image using the $(0\bar{1}2)$ reflection is given in Fig. 2(e). The dark domains in Fig. 2(c) appeared as bright domains in Fig. 2(e). Thus, there are two distinct crystalline domains in the MnSi layer that occur with nearly equal probability. In Fig. 3 we show that these domains result from the lack of inversion symmetry in the crystal structure. The B20 structure twists the lattice sites away from a centrosymmetric configuration and leads to a handedness in the crystal structure. A right-handed stacking of the Mn planes is referred to in the literature as a right-handed crystal structure.[25] Presented in Fig. 3 are the results of a 25-beam, dynamical Bloch wave simulation of diffraction pattern intensities at the [221] zone-axis orientation for MnSi with a right-handed chirality where only the intensities of the $(\bar{1}02)$ and $(0\bar{1}2)$ beams are plotted as a function of specimen thickness. It is observed that the $(\bar{1}02)$ beam is much more intense than the $(0\bar{1}2)$ beam, as was the case for the SADP shown in Fig. 2(b). If an inversion operation is performed on the atoms in the unit cell so that the right-handed chiral structure becomes left handed, then the intensities in the two beams plotted in Fig. 3 reverse and we would expect to observe the SADP as shown in Fig. 2(d). The origin of the contrast between the two chiral domains is the large difference in structure factors associated with the $(\bar{1}02)$ and $(0\bar{1}2)$ reflections. Inverting the B20 crystal structure reverses these two structure factors, leading to reversed image contrast as observed in Fig. 2(e). Therefore we conclude that there are both left- and right-handed chiral domains present in our MnSi layers.

Figure 4 shows a HRTEM image of an 11.5-nm-thick MnSi layer, where the interface between the MnSi layer and Si substrate is viewed along the $[11\bar{2}]$ and [110] zone-axis orientations, respectively. The crystalline quality of the MnSi epilayer is excellent and the only crystalline defects observed are misfit edge dislocations at the MnSi-Si interface with a Burgers vector of $\mathbf{b}=a_{\text{MnSi}}[\bar{1}10]/2$, similar to MnSi films grown on an MnSb interfacial layer on Si(111).[26] The inset is a HRTEM simulation of MnSi confirming the observed image contrast.[27] The 11.5-nm-thick MnSi film has approximately a 1 nm roughness (rms), as determined from lower magnification cross-sectional images, which is consistent with model fits to the XRR data.

The in-plane tensile stress causes a Poisson contraction of the MnSi (111) planes, which was measured by XRD using a Siemens D500 diffractometer equipped with a Cu target tube and a monochromator. The θ-2θ scans in the angular range from 10° to 80° confirmed that the films were epitaxial with MnSi(111)$\|$Si(111). The Si (111) and Si (222) diffraction peaks from the substrate were used to provide an accurate calibration of the peak position of MnSi (111), which was used to determine the out-of-plane strain, $\varepsilon_{\perp}$. An unusual, nonmonotonic variation in $\varepsilon_{\perp}$ with thickness, which decreases with increasing thickness up to 7 nm before relaxing, is shown in Fig. 5(b). Insight into this behavior may be obtained by calculating the ratio of the strains, $-\varepsilon_{\perp}/2\varepsilon_{\|}$, which is plotted in Fig. 5(c). The MnSi films show considerable departure from the value of 0.19 as calculated from the elastic stiffness constants for bulk MnSi, $c_{11}=283.3$ GPa, $c_{12}=64.1$ GPa, and $c_{44}=117.9$ GPa,[28] using the expression derived in Ref. 29 for (111) oriented films,

$$-\frac{\varepsilon_{\perp}}{2\varepsilon_{\|}} = \frac{c_{11}+2c_{12}-2c_{44}}{c_{11}+2c_{12}+4c_{44}}. \qquad (2)$$

The variation in this quantity indicated that elastic constants in the MnSi film changed as a function of thickness. From Eq. (2), we determine the ratio of the shear elastic constant c_{44} to the compressibility $\kappa=(c_{11}+2c_{12})/3$ and observed that c_{44}/κ decreases linearly from 1.06 at 4 nm, to $c_{44}/\kappa=0.63$ at 10 nm, as compared to 0.93 expected from bulk elastic constants.

The elastic constants of thin films are known to deviate significantly from bulk values and defects generally lead to a softening of the elastic constants. It is possible that the observed atypical elastic behavior of the MnSi films was due to softening of c_{44}. A softening of c_{44} is consistent with a softening of the elastic stiffness constant corresponding to the [111] direction, $c'_{33}=(2c_{11}+2c_{12}+c_{44})/4$. These observations are comparable to those reported for Fe films on Si (100),[30] where the thickness dependence of the out-of-plane elastic constant and out-of-plane strain showed trends similar to

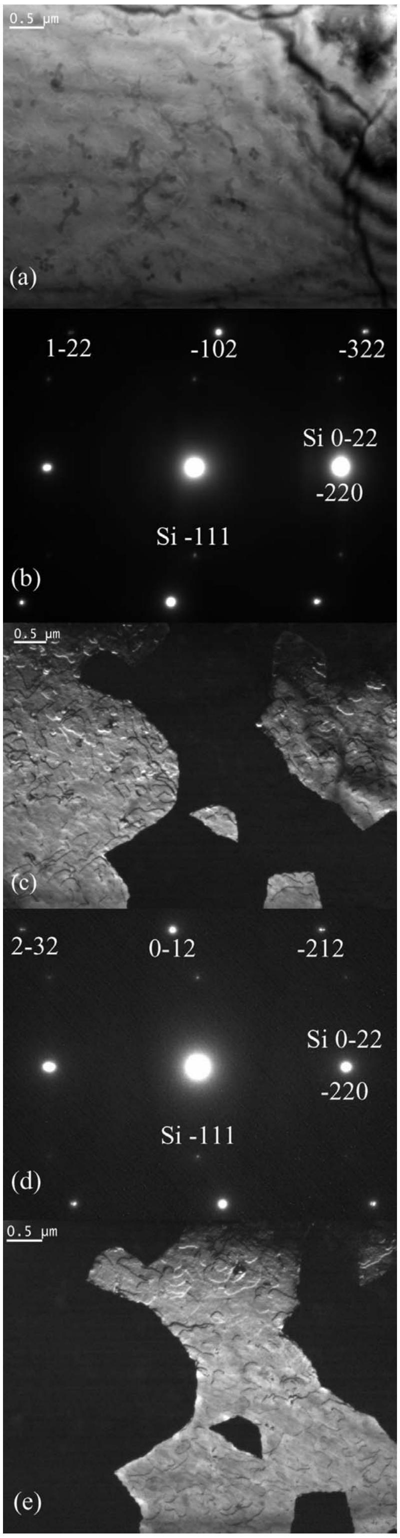

FIG. 2. (a) Plan-view bright-field TEM image of a 6-nm-thick MnSi layer on a Si substrate at the MnSi [221] zone-axis orientation. The debris on the surface is due to polishing residue since the specimens were not ion milled. (b) SADP from one of the MnSi chiral domains. (c) Dark-field TEM image using the ($\bar{1}02$) spot from (b). (d) SADP from the opposite MnSi chiral domain. (e) Dark-field TEM image using the ($0\bar{1}2$) spot from (d). The strong line contrast in Figs. 2(c) and 2(d) was due to threading dislocations.

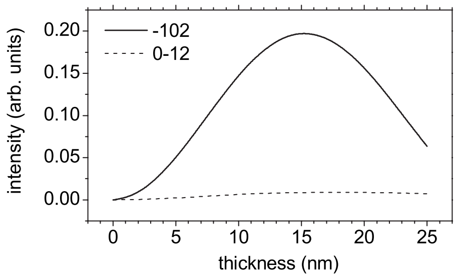

FIG. 3. Bloch-wave diffracted beam intensities plotted as a function of MnSi thickness for the conditions of Fig. 2(b).

c_{44}/κ and $\varepsilon_{\perp}$. One possible defect that may be responsible for the observed behavior is interstitials. Interstitial defects are known to have a large influence on the elastic constants: c_{44} of single-crystal Cu drops by as much as 31% per atomic percent of interstitials, with a negligible change in the κ.[31] Therefore a few atomic percent of interstitials may be sufficient to cause the variations observed in Fig. 5(c).

III. MAGNETIC PROPERTIES

A. Static magnetic properties

The magnetic properties were measured with a Quantum Design MPMS-XL SQUID magnetometer configured with a longitudinal pick-up coil. The applied dc and ac fields were oriented along the MnSi [$1\bar{1}0$] direction for all measurements, unless otherwise noted. The atypical thickness dependence of the strain found in these MnSi thin films raises the question of how this correlates with T_C. The Curie temperature was determined using two different methods: (1) from measurements of the remanent magnetization, M_r, and (2) from the field-cooled (FC) magnetization as a function of temperature. In Fig. 6(a), we show the temperature dependence of M_r measured following saturation of the sample in a field of 5 T at a temperature of 2 K. The unexpected shape of the magnetization curves is addressed in the context of the

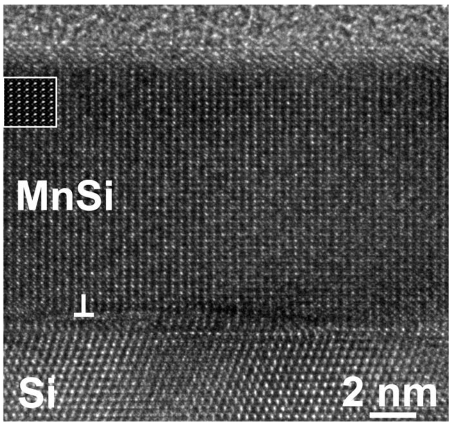

FIG. 4. HRTEM image of an 11.5-nm-thick MnSi layer on Si at the [$11\bar{2}$] and [110] zone-axis orientations, respectively. The location of a misfit edge dislocation ($\mathbf{b}=a_{\mathrm{MnSi}}[\bar{1}10]/2$) in the MnSi has been highlighted and a HRTEM image simulation of MnSi has been inset.

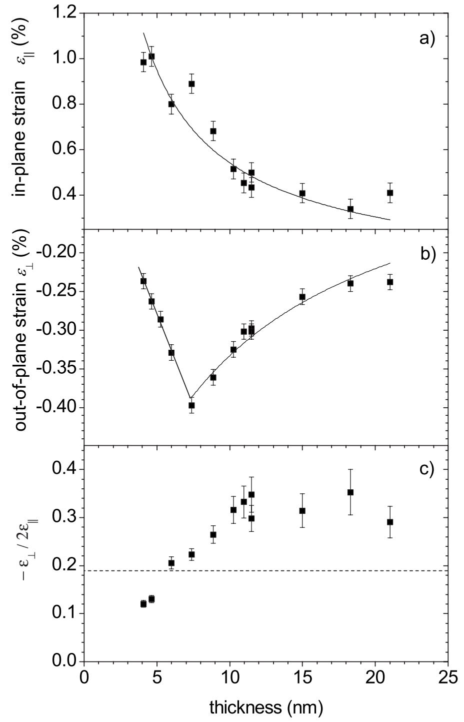

FIG. 5. (a) The in-plane strain measured by TEM plan-view selected-area diffraction patterns. (b) The out-of-plane strain measured by XRD. (c) The ratio of the out-of-plane to twice the in-plane strain. The dashed line indicates the value expected from bulk elastic constants.

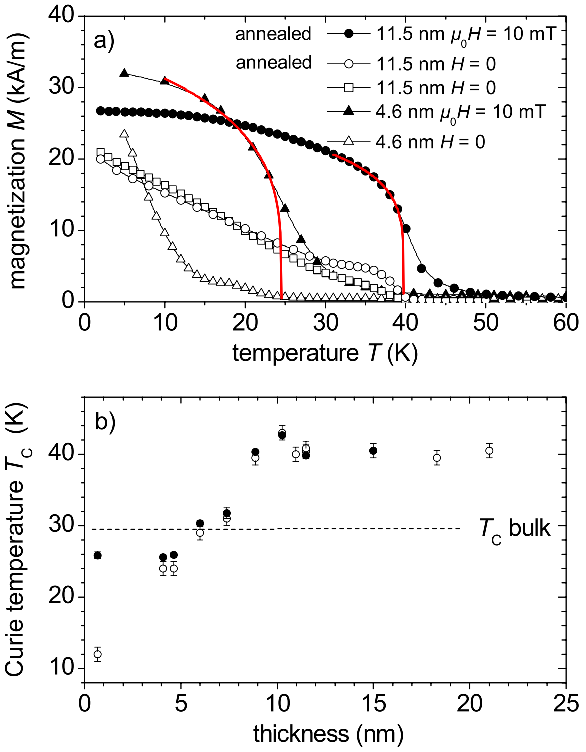

FIG. 6. (Color online) (a) The open symbols show the remanent magnetization of MnSi films, measured on warming the sample. The filled symbols show the field-cooled magnetization together with power-law fits, shown by the thick solid lines. The data labeled annealed corresponds to a sample that was heated *ex situ* at 400 °C for 1 h. (b) The Curie temperature measured as a function of film thickness determined from the remanent-magnetization (open circles) and from field-cooled magnetization measurements (filled circles).

magnetic dynamics in Sec. III B. The point where the magnetization goes to zero gives a measure of T_C, which is plotted as a function of thickness in Fig. 6(b). This is determined from the knee in the M_r-versus-T plots: the M_r a few degrees below T_C is extrapolated to the temperature where it is equal to the measured background magnetization, which is on the order of 0.1 kA/m, corresponding to a total background moment of 10^{-11} Am^2. Since magnetic domains can obscure the measurement of T_C, we also measured the samples by first cooling them from 90 to 5 K in an applied field of 0.010 mT and then measured the magnetization in the applied field on warming. Two examples of this measurement, along with power-law fits to the data close to T_C are shown in Fig. 6(a). The filled circles in Fig. 6(b) indicate T_C obtained from the power-law fits. Both methods of determining T_C are in agreement, with the exception of the 0.7 nm sample, where the magnetic domain structure likely caused the low value of T_C obtained from the M_r. T_C in the films drops at lower film thickness, as would be expected due to finite-size scaling.[32] The transition temperature in thin magnetic films is smeared and lowered because the reduced dimension in the film restricts the divergence of the spin-spin correlation length, although one would have expected the drop in T_C to occur over a shorter thickness range in MnSi given the measurements on Fe, Co, Ni,[33,34] and Gd.[35]

In an attempt to separate the finite-size effects from the strain effects, we compare our results with measurements on bulk MnSi under hydrostatic pressure. Although the stress in the film is not hydrostatic, it is speculated that T_C will have a similar dependence on volume strain $\Delta V/V_0$ for both hydrostatic and biaxial stress. We are not aware of any calculations of the effects of biaxial strain on MnSi but density-functional calculations of GdN indicate that changes in band structure are similar for both hydrostatic and biaxial stress due to a small Poisson ratio of 0.2 (Ref. 36) whereas the Poisson ratio for bulk MnSi is $c_{12}/(c_{11}+c_{12})=0.185$. The pressure dependence of T_C from Ref. 37 was converted to $\Delta V/V_0$ using a bulk modulus of $\kappa=(c_{11}+2c_{12})/3 = 137$ GPa and plotted in Fig. 7(a). Reference 37 fits T_C using Moriya's spin fluctuation theory, $T_C \sim (p_c-p)^{3/4}$, which we use to extrapolate the bulk data to positive strain to give an estimate of T_C in the infinitely thick film limit. Whereas the fit is good over a range of $\Delta V/V_0$ from 0 to -1×10^{-4} in bulk, we would expect that the extrapolation should be reasonable at least to $\Delta V/V_0=+1\times10^{-4}$. The extrapolation of the bulk data fits T_C of the films well for thickness greater than 10 nm, which corresponds to $\Delta V/V_0<7\times10^{-5}$. In Fig. 7(b), the deviation of $T_C(n)$ of film from the extrapolated bulk value, $T_C(\infty)$, is calculated and plotted. For comparison with the work done on ferromagnetic thin films, we plot T_C as a function of the number of monolayers, n, where we defined 1 ML = 0.263 nm, the MnSi (111) plane spacing. In the case of Ni and Gd films, a simple model interprets the effects of finite size on T_C as resulting from the reduction in

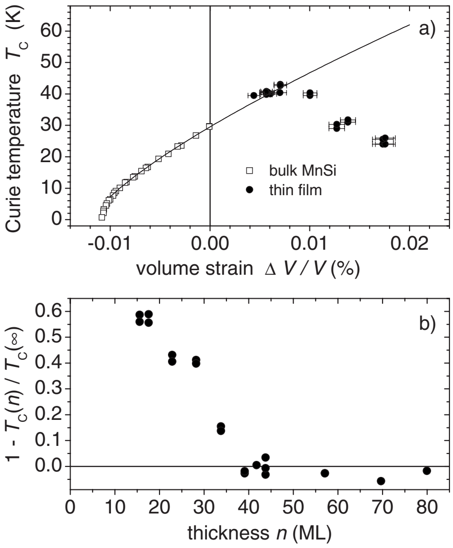

FIG. 7. (a) Comparison between the dependence of Curie temperatures on volume strain in MnSi thin films and the data for bulk MnSi from Ref. 37. The curve is an extrapolation of a fit to the bulk data using spin-fluctuation theory. (b) The normalized difference between extrapolated bulk $T_C(\infty)$ and measured $T_C(n)$.

the number of pairwise spin-spin interactions due to the presence of the film's interfaces.[34] The thickness range over which a reduction in T_C is observed is given by the range of the exchange interaction. However, this model would require the spin-spin interactions in MnSi to extend over 20 ML to explain the slow linear decay in $1-T_C(n)/T_C(\infty)$, which is considerably larger than 5 ML for Ni and 8.6 ML for Gd.[34] The strong correlation between $-\varepsilon_\perp/2\varepsilon_\parallel$ and T_C suggests that changes in the elastic constants and the critical temperature with thickness have a common origin, possibly point defects. Interstitial defects, which provide an explanation for the change in elastic constants discussed in Sec. II are also know to have a large effect on T_C of magnetic materials.[38] Si or Mn interstitials resulting from solid-phase epitaxy may be responsible for the observed behavior. *Ex situ* annealing at 400 °C for 1.5 h resulted in only modest changes to the defects present in the film and annealing times much longer were avoided to prevent the formation of higher silicides. The peak in the ac susceptibility in Fig. 11, to be discussed in the following section, became sharper with annealing. However, the *ex situ* annealing step did not significantly change T_C, although some changes in the shape of the $M_r(T)$ curves are visible in Fig. 6(a). This suggests that the annealing did not significantly affect the defects in the film.

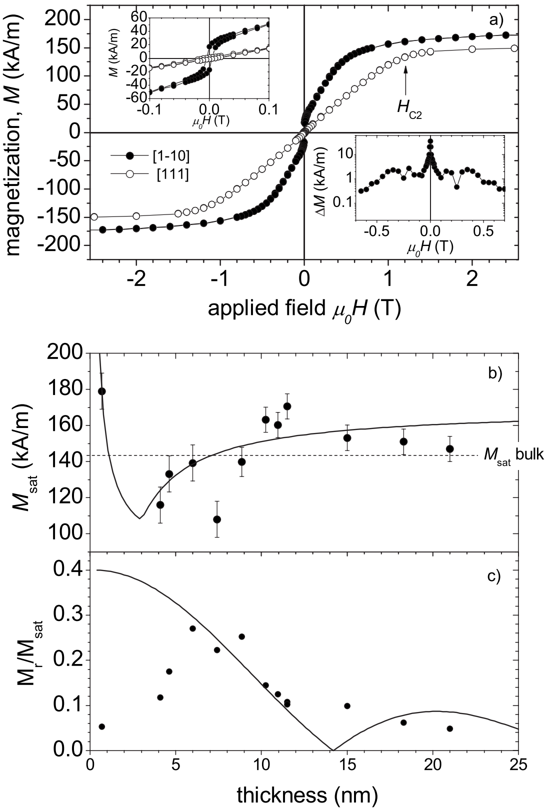

FIG. 8. (a) Magnetization curves (M versus H) measured at 5 K for an 11.5-nm-thick sample. The upper inset shows the magnetization between $\mu_0H=-0.1$ and 0.1 T. The lower inset is the difference between the in-plane M-H curves for increasing and decreasing H, which shows that hysteresis extends to fields of approximately 0.5 T. (b) The saturation magnetization as a function of MnSi thickness. The solid line is a fit to the data, as described in the text. The dashed line is M_{sat} for bulk MnSi. (c) The remanent magnetization normalized to the saturation magnetization as a function of MnSi thickness. The solid line is the expected dependence obtained from Eq. (3) assuming helical magnetic order with $\mathbf{Q}\|[111]$ and a wavelength $2\pi/Q=14$ nm.

Hysteresis curves were measured in order to address the question of the magnetic structure of the films. The diamagnetic response of the Si substrate gave a large linear background to the measured M-H curves. This diamagnetic background could not be easily separated from the response of the MnSi film because at low temperatures and fields above 0.6 T the magnetization of bulk MnSi increases linearly with a small high-field susceptibility, $\chi_{\mathrm{HF}}=1.69$ kA/m/T, with no sign of saturation below 14 T.[39] Since the increase in magnetization due to χ_{HF} is small compared to the extrapolated high-field magnetization of 1.5×10^2 kA/m, we neglect it and assign the slope of the M-H curve between 3.0 and 5.0 T to the susceptibility of the substrate and subtract it from the data. Although this correction procedure underestimates the susceptibility of the substrate, the correction from χ_{HF} is expected to be only 2% at a field strength of 2 T, and does not affect the measurement of M_r, nor the saturation magnetization, M_{sat}, obtained by extrapolation of the high-field portion of the M-H curves to $H=0$.

We find that the shape of the M-H curves is consistent with those of bulk crystals with helical magnetic order. The open circles in Fig. 8 are out-of-plane measurements, where the applied field is parallel to the direction that $\mathbf{Q}$ points in bulk MnSi. The M-H curves are qualitatively similar to those reported in bulk:[39,40] the open circles in Fig. 8(a) show that the magnetization increases approximately linearly with applied magnetic field up to a critical field of 1.16 ± 0.01 T, obtained from the minimum in $\partial^2M/\partial H^2$, which we assign to the field required to induce a saturated ferromagnetic state, labeled H_{C2} in bulk. For in-plane hysteresis measurements along $[1\bar{1}0]$, the M-H features were qualitatively similar to the out-of-plane measurement, although they were more rounded than the out-of-plane measurements, as shown in Fig. 8(a). The saturation magnetization of bulk MnSi extracted from the *M*-*H* curves is shown by the dashed line in the Fig. 8(b) and corresponds to the bulk moment of 0.39 μ_B/Mn.[39] For films thicker than 10 nm, the films exhibit a magnetization consistent with bulk material. As the film thickness decreases below 10 nm, the magnetization drops before rising to a value greater than the bulk. The enhanced moment for the thinnest films is likely an effect from the interfaces, as density-functional theory (DFT) calculations predict a moment of 3.4 μ_B/Mn at a MnSi/Si interface.[41] With increasing film thickness there is a drop in the moment per Mn atom, which we attribute to the defects that create the changes in the elastic properties and T_C. We are able to describe M_{sat} by modeling the MnSi film with four layers: a defected MnSi layer near the substrate, and bulk-like MnSi layer above it, and the two MnSi/Si interfaces, which are assumed for simplicity to be the same. We treated the moments in all three regions as fitting parameters, in addition to the defect layer thickness, and present the result by the solid line in Fig. 8(b). In contrast to a large moment predicted by DFT, we obtain a MnSi/Si interfacial moment of (0.5 ± 0.1) μ_B/Mn. The defected layer is (3 ± 1) nm thick with a moment of (0.22 ± 0.09) μ_B/Mn and the moment of the bulklike layer is (0.43 ± 0.03) μ_B/Mn.

While M_{sat} of the films is comparable to the bulk value, H_{C2} is considerably larger than the bulk value of 0.6 T. Part of this difference is due to the demagnetizing field, $\mu_0 H_D$ of the thin-film samples, which is $\mu_0 M_{\text{sat}}=0.19\pm0.07$ T for the samples thicker than 11 nm. Subtracting this contribution gave an intrinsic critical field of $H_{C2}^{\text{int}}=0.97\pm0.7$ T. Given that $H_{C2}\cong AQ^2$,[42] where *A* is the exchange stiffness, the larger H_{C2}^{int} in the films could be explained by a reduction in the wavelength of the helix to 14 ± 1 nm, assuming that *A* does not change significantly from the bulk value.

One interesting question is whether helical magnetic order survives in thin films. The M_r extracted from the *M*-*H* curves provided an indirect measure of the magnetic structure. The top inset of Fig. 8(a) shows that a remanent magnetization exists for in-plane measurements whereas the out-of-plane M_r is zero to within experimental error, given the ±5° uncertainty in the alignment of the sample in the SQUID magnetometer. The presence of an in-plane M_r is consistent with a helical magnet whose magnetic moments are in-plane and spiral about an out-of-plane propagation wave vector. For **Q** pointing out-of-plane, there is incomplete cancellation of the magnetic moments when the thickness is not an integer multiple of wavelengths, $2\pi/Q$. This fact should enable a determination of $2\pi/Q$, assuming that **Q** is along [111]. In Fig. 8(c), we plot M_r normalized to M_{sat} as a function of thickness and compare it to M_r obtained by integration of the moments of the helical magnet over a distance equal to the film thickness, *d*,

$$M_r=\frac{2M_{\text{sat}}}{Qd}\sin\left(\frac{Qd}{2}\right), \tag{3}$$

with the wavelength predicted from the hysteresis measurements, $2\pi/Q=14$ nm. We find that the size of M_r is considerably smaller than expected from the integration of the moments of the helical magnet over a distance equal to the film thickness. This difference is attributed to the presence of magnetic domains, which will be discussed in Sec. IV, and the calculated curve was rescaled by a factor of 0.4 for better comparison with the data. There is a large difference between the data and the model below $d=7$ nm, which may be due to the presence of defects suggested by the measurements of strain and T_C over the same range of thicknesses. However, the remanent magnetization does not go to zero for any *d*, contrary to the expectations for a helical magnet. The rounded features in the *M*-*H* curves relative to bulk suggest that there are inhomogeneities in the films, possibly creating a distribution of helical wavelengths. These inhomogeneities together with variations in *d* due to roughness could be obscuring the oscillations in M_r with thickness.

B. Dynamic magnetic properties

The dynamical and temperature dependence of the magnetization exhibit an unexpected glassy behavior. Therefore, we have performed a number of measurements to determine the origin of this glassy behavior and to test whether a thin film of MnSi is a reentrant spin glass. Spin glasses result from the effects of disorder and frustration, and lead to a variety of nonequilibrium phenomena. Standard measurements of spin glasses include field-cooled (FC) and zero-field-cooled (ZFC) magnetization measurements to determine the onset of the nonequilibrium behavior. In thermoremanent magnetization (TRM) measurements, the sample is cooled in an applied field, and then the decay of the magnetization after waiting a certain time before turning off the field is measured. In spin glasses this decay is sensitive to the wait time, which is known as aging. These slow dynamics also manifest themselves as a frequency dependence of the ac susceptibility and a divergence of the nonlinear susceptibility. While reentrant helical spin-glass behavior was reported in a similar B20 structure, $\text{Cr}_{0.81}\text{Mn}_{0.19}\text{Ge}$,[43] the authors did not demonstrate that their material satisfied all of the above criteria. We will demonstrate that our MnSi films are not spin glasses and the glassy behavior can be explained by a broad distribution of energy barriers.

ZFC measurements shown in Fig. 9 were made after warming the sample to 90 K, well above T_C, and then cooling the sample to 2 K prior to applying a field. The FC measurements followed the same temperature program. Plots of the differences between the ZFC and FC data were used to determine the temperature where the bifurcation in the magnetization occurred, T_{irr}, which signaled the onset of irreversibility. T_{irr} was linear as a function of field between 5 mT and 0.5 T. The bifurcation, however, is not unique to spin glasses. Ferromagnets with a large coercivity can also display this behavior. Although the coercivity of our films is very small, approximately 5 mT, the hysteresis extends to high field, as shown by the lower inset of Fig. 8(a). The disappearance in the hysteresis in the *M*-*H* loops coincides well with the disappearance of hysteresis in the FC-ZFC measurements and we find that $T_{\text{irr}}=5$ K corresponds to a field of 0.47 T, in good agreement with the lower inset of Fig. 8(a).

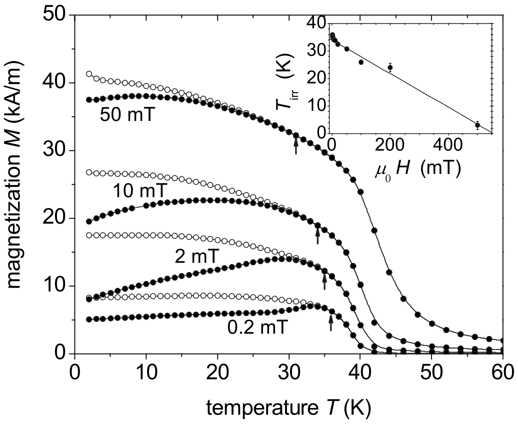

FIG. 9. The ZFC (solid points) and FC (open points) magnetization curves measured in various fields for an 11.5-nm-thick MnSi layer. The arrow indicates T_{irr} where the ZFC measurement begins to deviate from the FC that was obtained from plots of the difference in the FC and ZFC magnetization. The inset shows T_{irr} as a function of the applied field.

A second test of the glassy behavior is the TRM measurements, which reveal that the magnetization relaxed over very long-time scales. The data were collected by cooling the sample from 90 K to a target temperature in a field of 10 mT. Once the target temperature was reached, we waited a time, $t_{\mathrm{w}}=500$ s, before turning off the field. The remanent magnetization $M_{\mathrm{r}}(t)$ was measured at a fixed temperature as a function of time, t, from the instant the current in the magnet reached zero. For most temperatures the time dependence of the TRM, $M_{\mathrm{r}}(t)$, is well described by the phenomenological equation,

$$M_{\mathrm{r}}(t) = M_0 - S\ln(t), \tag{4}$$

where M_0 is a constant and S is the magnetic viscosity. However, there are departures from this functional form when T is near 30 K, as seen in Fig. 10(a). In order to avoid these departures in the fitting, fits to the TRM data are restricted to the interval where $S=-dM_{\mathrm{r}}(t)/d\ln(t)$ is constant, $10^3 < t < 10^4$ s, and the results are plotted in Fig. 10(b), which shows a broad peak at 27 K. The logarithmic time dependence in Fig. 10(a) and the broad peak in the viscosity both indicate that the magnetization relaxes over a broad distribution of energy barriers. As a test for spin-glass behavior, we repeated the measurements for a range of wait times, $500 \leq t_{\mathrm{w}} \leq 5000$ s, at a temperature near the peak of the viscosity. All of the experiments were found to be independent of t_{w} and no aging phenomena were observed, in contrast to the behavior expected from canonical spin glasses.

However, some of the unexpected behavior of the remanent magnetization is explained by the TRM measurements. The linear dependence of the $M_{\mathrm{r}}(T)$ curves in Fig. 6(a) was unexpected given that the staggered magnetization in bulk MnSi follows $[M(0)-M(T)] \sim \mathrm{T}^{3/2}$, as explained by spin-fluctuation theory.[44] The authors are not aware of a spin-wave theory in the thin-film limit for helical magnets, which is needed for a detailed comparison with $M_{\mathrm{r}}(T)$. However, some insight can be gained from the theory for ferromagnets.

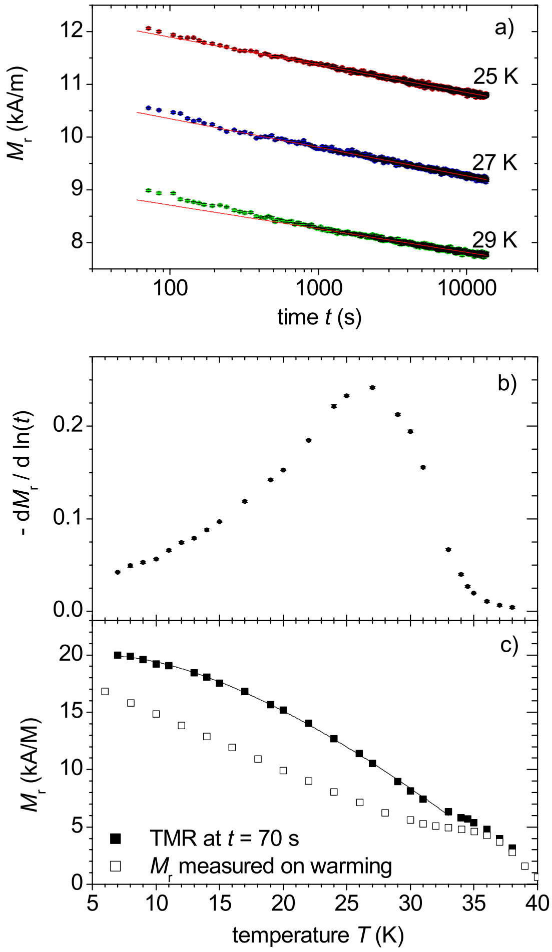

FIG. 10. (Color online) (a) TRM in a 11.5-nm-thick MnSi film as a function of time, t, measured after cooling in an applied field of 10 mT, and waiting for $t_{\mathrm{w}}=500$ s at the target temperature before turning off the field. (b) The magnetic viscosity determined from the slope of the TRM data at 3600 s. (c) TRM measured approximately $t=70$ s after turning off the field. The curve is a fit using spin-wave theory for ferromagnetic thin films, Eq. (5). For comparison, a portion of the M_{r}-T data from Fig. 6(a)) is included.

Similar to MnSi, the magnetization calculated from mean-field theory for ferromagnets also follows a $T^{3/2}$ law, as observed in a number of materials. In ferromagnetic thin films, the freezing out of spin waves with a wave vector along the film normal modifies the temperature dependence of the magnetization,

$$[M_{\mathrm{r}}(0) - M_{\mathrm{r}}(T)] \sim k_{\mathrm{B}}T\ln(E_{\mathrm{g}}/k_{\mathrm{B}}T), \tag{5}$$

where E_{g} is the effective spin-wave gap due to anisotropy and dipolar interactions.[45] In the case of MnSi thin films, the departure of $M_{\mathrm{r}}(T)$ from the form given by Eq. (5) can be understood with the aid of the TRM measured as soon as possible after the field was turned off and before the magnetization had a chance to relax significantly. The TRM measured at approximately $t=70$ s as a function of temperature in Fig. 10(c) is well described by Eq. (5) with $E_{\mathrm{g}}=1.4$ meV, and therefore the difference between the TRM

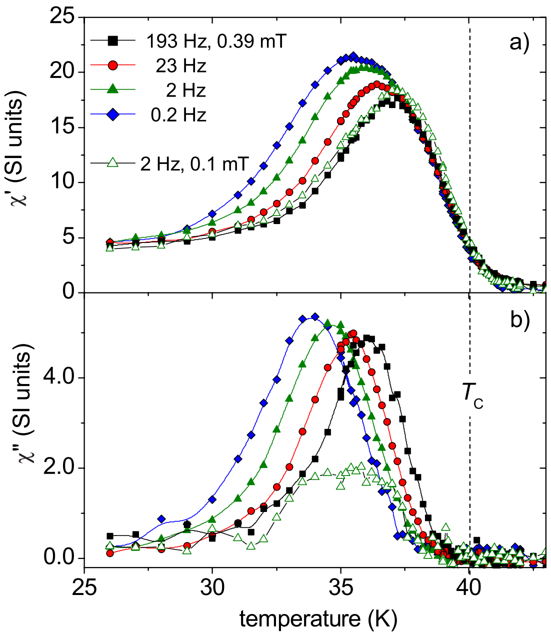

FIG. 11. (Color online) (a) The in-phase and (b) the out-of-phase components of the ac susceptibility for an 11.5-nm-thick MnSi film. The filled circles show the dependence of the susceptibility on the frequency for a drive field of $h_{ac}=0.39$ mT. The open circles correspond to $h_{ac}=0.10$ mT and $f=2.0$ Hz.

and $M_r(T)$ curves can be understood by the slow decay of the magnetization.

As a final test for the presence of glassy behavior, ac-susceptibility measurements were performed in the frequency range from $0.2 \leq f \leq 1000$ Hz to probe the magnetic relaxation on time scales that were many orders of magnitude shorter than the TRM. There is not a peak in the ac susceptibility at $T_C=40.5$ K in Fig. 11, as expected from bulk measurements at ambient pressure. Although many properties of bulk MnSi appear consistent with a second-order transition, heat-capacity,[46] and neutron-diffraction experiments[47] show that the transition is weakly first order. However, the films show neither a discontinuity in χ nor M_r at T_C that would indicate a first-order transition. Given the ambiguity of the transition in bulk, it is perhaps not surprising that our measurements are not able to identify the order of the phase transition in MnSi films. A combination of finite-size scaling effects and inhomogeneity of the film thickness likely broadens the phase transition and obscures the signatures that are present in bulk measurements.

Below T_C, a peak does appear in the ac susceptibility, $\chi=\chi' + i\chi''$. When the ac-drive field is $h_{ac}=0.1$ mT, the nonlinear response is small and the peak in the dissipative component of the susceptibility, χ'', is wide, which implies a broad distribution of energy barriers. For large drive fields, this peak increases in intensity. Because of the relatively small signal, we investigated the frequency dependence of χ with an $h_{ac}=0.39$ mT and found that the peak shifts to higher temperature with increasing frequency, similar to the response of perpendicularly magnetized Fe films.[48] For the Fe films, a single activation energy is able to provide a good fit to the data. However, because of the broad distribution of energy barriers implied by the broad peak in χ'', a fit of the dependence of T_p on frequency to an Arrhenius law, $\tau=\tau_0 \exp(T_a/T)$, with a single activation temperature, T_a, yields unphysical values of $\tau_0=10^{-49}$ s and $T_a=3.86\times 10^3$ K. A similar failure of the Arrhenius law is observed for spin glasses. For spin glasses, the frequency dependence of T_p is often quantified by $(\Delta T_p/T_p)$ per decade of angular frequency, ω, which serves as means of distinguishing spin-glasslike materials from true spin glasses. The figure of merit obtained for MnSi films from Fig. 11(b), $(\Delta T_p/T_p)/[\Delta(\log \omega)]=0.021$, was a little larger than that for the canonical metallic spin glasses (0.005–0.018) but smaller than the insulating spin glasses with values around 0.06.[49]

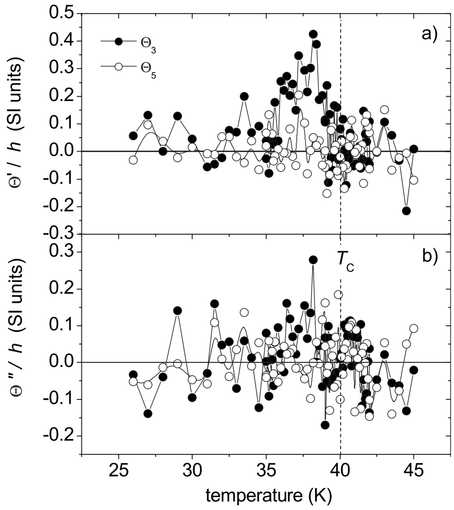

FIG. 12. The real (top) and imaginary (bottom) components of the third and fifth-order harmonics of the ac susceptibility of an 11.5-nm-thick MnSi film measured with $h_{ac}=0.10$ mT and $f=2.0$ Hz.

While ac susceptibility is commonly used to study spin glasses, and provides useful insight into the dynamics, it does not couple directly to the spin-glass order parameter. A more rigorous test of spin-glass behavior is a measure of the nonlinear susceptibility, $\chi_3=\partial^3 M/\partial H^3$, which diverges at the glass transition, analogous to the divergence in $\chi=\partial M/\partial H$ at a second-order paramagnetic-to-ferromagnetic transition.[50] In order to obtain χ_3, we extracted the harmonics of the SQUID output voltage from the ac-susceptibility measurements. The harmonics, Θ_n, of the SQUID signal are related to the true susceptibilities,[50]

$$\Theta_3 = \frac{1}{4}\chi_3' h_{ac}^3 + \frac{5}{16}\chi_5' h_{ac}^5 + \cdots,$$

$$\Theta_5 = \frac{1}{16}\chi_5' h_{ac}^3 + \frac{7}{64}\chi_7' h_{ac}^7 + \cdots, \tag{6}$$

where Θ_3 is the third harmonic ($3f$ response) and Θ_5 is the fifth. From Eq. (6) we obtained an estimate of $\frac{1}{4}\chi_3' h_{ac}^2$ by a measurement of $\Theta_3 - 5\Theta_5$. The small peaks in these harmonics shown in Fig. 12 cancel to give $\chi_3'=0$, and similarly for the imaginary component, χ_3''. The absence of a divergence in

χ_3'' rules out the existence of a reentrant spin-glass transition for temperatures above 5 K in the MnSi films.

IV. DISCUSSION

While there are many qualitative similarities between the data presented and data reported for bulk MnSi, the glassy behavior represents a clear departure from bulk properties. There are two important structural differences between films and bulk that point to sources of this behavior. The first are defects near the interface proposed in Sec. II to explain the elastic properties and T_C of the thinner films. The second important difference is the presence of inversion domains in the film. If the films do have helical order, then they must possess two magnetic chiralities since the handedness of the helical order is tied to crystal chirality: in bulk MnSi, left-handed inversion domains have a left-handed spiral.[25] The size of the inversion domains places an upper limit of a few microns on the lateral dimension of the magnetic domains. The interface between the two chiral domains would produce magnetic frustration due to competing windings of the magnetic moments. In the absence of defects and neighboring domains, the remanent magnetization could point in any in-plane direction due to the zero cubic magnetocrystalline anisotropy of the (111) plane. The glassy magnetic behavior can then be understood as a product of disorder and frustration in the films. The disorder arises from the distribution of inversion domains and defects, and the frustration comes from the inversion domain boundaries.

The following picture may then explain the peak in the ac-susceptibility curves. At temperatures near T_C there is little dependence of χ' on h_{ac}, which we attribute to the free motion of the domain walls that have little dissipation. As the temperature lowers, the energy barriers with the largest activation energies become resonant with the drive field resulting in an increase in the dissipative component, χ''. Upon further decrease in temperature, these domains become frozen as their relaxation times become long compared to the inverse of the drive frequency, and χ'' decreases. The ac-magnetic response from striped domains in perpendicularly magnetized Fe ultrathin films[48] was qualitatively similar to the response reported here for MnSi, although with a much narrower distribution of energy barriers. However, χ' does not go to zero at low temperature as in the case for the Fe films. The nonzero χ' is indicative of a component of the magnetization that is transverse to the ac-drive field, h_{ac}, as expected for a helical magnet.

V. CONCLUSION

In conclusion, we demonstrate a correlation between the structure and the magnetic properties of epitaxial MnSi (111) films on Si (111). We find that epitaxially induced strain in the films causes a volume expansion of the MnSi lattice. For films thicker than 10 nm, the increase in cell volume is consistent with the increase in T_C expected from bulk studies, assuming that the effects of biaxial stress and hydrostatic stress are similar in MnSi. At lower film thickness, however, departures from the expected behavior included a drop in M_{sat} and in T_C that could not be explained by finite-size scaling arguments. These are strongly correlated with the changes in the strain ratio $\varepsilon_\perp/\varepsilon_\parallel$. We propose that interstitial defects could explain both the observed changes in the elastic and magnetic properties of the films. While the M-H curves are consistent with bulk measurements, the thickness dependence of M_r did not show clear evidence of helical magnetic order, possibly because the oscillations in M_r are obscured by inhomogeneities and magnetic domains.

The films possess structural inversion domains that are a few microns in size, which implies that there should be left- and right-handed magnetic chiral domains. We attributed the glassy magnetic behavior to frustration between magnetic chiral domains. While the observed glassy magnetic behavior is similar to other reported spin glasses, the existence of a reentrant spin glass is ruled out due to the absence of a divergence in the nonlinear susceptibility and the absence of aging phenomena.

ACKNOWLEDGMENTS

This work was supported by the Natural Science and Engineering Research Council of Canada and the Canada Research Chairs Program. In addition, the authors gratefully acknowledge the support received from G. Botton and the Canadian Centre for Electron Microscopy. We would like thank A. Enders, R. Dunlap, and D. J. W. Geldart for useful discussions.

---

[1] J. Heurich, J. König, and A. H. MacDonald, Phys. Rev. B **68**, 064406 (2003).

[2] O. Wessely, B. Skubic, and L. Nordstrom, Phys. Rev. Lett. **96**, 256601 (2006).

[3] M. Lee, W. Kang, Y. Onose, Y. Tokura, and N. P. Ong, Phys. Rev. Lett. **102**, 186601 (2009).

[4] S. Mühlbauer, B. Binz, F. Jonietz, C. Pfleiderer, A. Rosch, A. Neubauer, R. Georgii, and P. Böni, Science **323**, 915 (2009).

[5] A. Neubauer, C. Pfleiderer, B. Binz, A. Rosch, R. Ritz, P. G. Niklowitz, and P. Böni, Phys. Rev. Lett. **102**, 186602 (2009).

[6] J. E. Jørgensen and S. E. Rasmussen, Powder Diffr. **6**, 194 (1991).

[7] Y. Ishikawa, G. Shirane, J. A. Tarvin, and M. Kohgi, Phys. Rev. B **16**, 4956 (1977).

[8] C. Thessieu, C. Pfleiderer, A. N. Stepanov, and J. Flouquet, J. Phys.: Condens. Matter **9**, 6677 (1997).

[9] C. Pfleiderer, S. R. Julian, and G. G. Lonzarich, Nature (London) **414**, 427 (2001).

[10] C. Pfleiderer, D. Reznik, L. Pintschovius, H. von Lohneysen, M. Garst, and A. Rosch, Nature (London) **427**, 227 (2004).

[11] Y. J. Uemura, T. Goko, I. M. Gat-Malureanu, J. P. Carlo, P. L. Russo, A. T. Savici, A. Aczel, G. J. MacDougall, J. A. Rod-

riguez, G. M. Luke, S. R. Dunsiger, A. McCollam, J. Arai, C. Pfleiderer, P. Böni, and K. Yoshimura, Nat. Phys. **3**, 29 (2007).

[12] B. Binz, A. Vishwanath, and V. Aji, Phys. Rev. Lett. **96**, 207202 (2006).

[13] U. K. Rößler, A. N. Bogdanov, and C. Pfleiderer, Nature (London) **442**, 797 (2006).

[14] S. Tewari, D. Belitz, and T. R. Kirkpatrick, Phys. Rev. Lett. **96**, 047207 (2006).

[15] J. Schmalian and M. Turlakov, Phys. Rev. Lett. **93**, 036405 (2004).

[16] M. M. R. Evans, J. C. Glueckstein, and J. Nogami, Phys. Rev. B **53**, 4000 (1996).

[17] S. Higashi, P. Kocan, and H. Tochihara, Phys. Rev. B **79**, 205312 (2009).

[18] S. M. Shivaprasad, C. Anandan, S. G. Azatyan, Y. L. Gavriljuk, and V. G. Lifshits, Surf. Sci. **382**, 258 (1997).

[19] Q. Zhang, M. Tanaka, M. Takeguchi, and K. Furuya, Surf. Sci. **507-510**, 453 (2002).

[20] A. Kumar, M. Tallarida, M. Hausmann, U. Starke, and K. Horn, J. Phys. D **37**, 1083 (2004).

[21] Y. C. Lian and L. J. Chen, Appl. Phys. Lett. **48**, 359 (1986).

[22] K. Schwinge, C. Müller, A. Mogilatenko, J. J. Paggel, and P. Fumagalli, J. Appl. Phys. **97**, 103913 (2005).

[23] E. Magnano, F. Bondino, C. Cepek, F. Parmigiani, and M. C. Mozzati, Appl. Phys. Lett. **96**, 152503 (2010).

[24] M. D. Robertson, T. Burns, and T. Morrison, Micros. Soc. Can. Bull. **34**, 19 (2006).

[25] M. Ishida, Y. Endoh, S. Mitsuda, Y. Ishikawa, and M. Tanaka, J. Phys. Soc. Jpn. **54**, 2975 (1985).

[26] K. Matsuda, H. Tatsuoka, K. Matsunaga, K. Isaji, H. Kuwabara, P. D. Brown, Y. Xin, R. Dunin-Borkowski, and C. J. Humphreys, Jpn. J. Appl. Phys., Part 1 **37**, 6556 (1998).

[27] J. M. Zuo and J. C. Mabon, Microsc. Microanal. **10**, 1000 (2004).

[28] S. M. Stishov, A. E. Petrova, S. Khasanov, G. K. Panova, A. A. Shikov, J. C. Lashley, D. Wu, and T. A. Lograsso, J. Exp. Theor. Phys. **106**, 888 (2008).

[29] D. Sander, Rep. Prog. Phys. **62**, 809 (1999).

[30] H. Ogi, M. Fujii, N. Nakamura, T. Shagawa, and M. Hirao, Appl. Phys. Lett. **90**, 191906 (2007).

[31] P. H. Dederichs, C. Lehmann, and A. Scholz, Z. Phys. B **20**, 155 (1975).

[32] M. E. Fisher and M. N. Barber, Phys. Rev. Lett. **28**, 1516 (1972).

[33] F. Huang, M. T. Kief, G. J. Mankey, and R. F. Willis, Phys. Rev. B **49**, 3962 (1994).

[34] R. Zhang and R. F. Willis, Phys. Rev. Lett. **86**, 2665 (2001).

[35] J. S. Jiang and C. L. Chien, J. Appl. Phys. **79**, 5615 (1996).

[36] C. G. Duan, R. F. Sabiryanov, J. J. Liu, W. N. Mei, P. A. Dowben, and J. R. Hardy, Phys. Rev. Lett. **94**, 237201 (2005).

[37] C. Pfleiderer, G. J. McMullan, S. R. Julian, and G. G. Lonzarich, Phys. Rev. B **55**, 8330 (1997).

[38] S. Yu. Dan'kov, A. M. Tishin, V. K. Pecharsky, and K. A. Gschneidner, Jr., Phys. Rev. B **57**, 3478 (1998).

[39] D. Bloch, J. Voiron, V. Jaccarino, and J. H. Wernick, Phys. Lett. A **51**, 259 (1975).

[40] K. Koyama, T. Goto, T. Kanomata, and R. Note, Phys. Rev. B **62**, 986 (2000).

[41] M. Hortamani, P. Kratzer, and M. Scheffler, Phys. Rev. B **76**, 235426 (2007).

[42] S. V. Maleyev, Phys. Rev. B **73**, 174402 (2006).

[43] T. Sato, T. Ando, T. Oku, and M. Furusaka, Phys. Rev. B **49**, 11864 (1994).

[44] K. Makoshi and T. Moriya, J. Phys. Soc. Jpn. **44**, 80 (1978).

[45] R. P. Erickson and D. L. Mills, Phys. Rev. B **44**, 11825 (1991).

[46] S. M. Stishov, A. E. Petrova, S. Khasanov, G. K. Panova, A. A. Shikov, J. C. Lashley, D. Wu, and T. A. Lograsso, Phys. Rev. B **76**, 052405 (2007).

[47] C. Pappas, E. Lelièvre-Berna, P. Falus, P. M. Bentley, E. Moskvin, S. Grigoriev, P. Fouquet, and B. Farago, Phys. Rev. Lett. **102**, 197202 (2009).

[48] D. Venus and M. J. Dunlavy, J. Magn. Magn. Mater. **260**, 195 (2003).

[49] J. A. Mydosh, *Spin Glasses: An Experimental Introduction* (Taylor & Francis, London, 1993).

[50] L. P. Lévy, Phys. Rev. B **38**, 4963 (1988).